3D acoustic least-squares reverse-time migration using the energy norm

Daniel Rocha, Paul Sava & Antoine Guitton
Center for Wave Phenomena, Colorado School of Mines

ABSTRACT

We propose a least-squares reverse time migration (LSRTM) method that uses an energy-based imaging condition to obtain faster convergence rates when compared with similar methods based on conventional imaging conditions. To achieve our goal, we also define a linearized modeling operator that is the proper adjoint of the energy migration operator. The proposed modeling and migration operators use spatial and temporal derivatives that attenuate acquisition artifacts and deliver a better representation of the reflectivity and of the scattered wavefields. We apply the method to two Gulf of Mexico field datasets: a 2D towed-streamer benchmark dataset and a 3D ocean-bottom node dataset. We show the LSRTM resolution improvement relative to RTM images, as well as the superior convergence rate obtained by the linearized modeling and migration operators based on the energy norm, coupled with inversion preconditioning using image-domain non-stationary matching filters.

Key words: least-squares migration, acoustic, 3D, ocean bottom node, Gulf of Mexico, reverse time migration

1 INTRODUCTION

Wavefield migration delivers an image of the subsurface structures using wavefield extrapolation methods (Sun et al., 2003; Biondi, 2012). For complex geological settings, the two-way wave equation is generally used for extrapolation and the migration procedure is known as reverse time migration (RTM) (Baysal et al., 1983; McMechan, 1983; Lailly, 1983; Levin, 1984; Zhang and Sun, 2009). In practice, however, data recording are always incomplete and possibly aliased and irregular, causing wavefield migration to degrade image quality and resolution especially for greater depths (Zhang et al., 2015). Such degradation occurs because migration represents the adjoint operator of single-scattering modeling, and therefore it is not a good approximation of the inverse operator that correctly reverses propagation of seismic data (Claerbout, 1992).

Considering these imaging quality issues, least-squares migration (LSM) is proposed to deliver images with more accurate amplitudes, illumination compensation, and reduced footprint of the acquisition geometry (Chavent and Plessix, 1999; Nemeth et al., 1999; Kuhl and Sacchi, 2003; Aoki and Schuster, 2009). If the RTM engine is used for migration, the method is called least-squares reverse time migration (LSRTM) (Dai et al., 2010; Yao and Jakubowicz, 2012; Dai and Schuster, 2012; Dong et al., 2012). Least-squares migration involves a forward operator (single-scattering modeling), an adjoint operator (migration), and an objective function which work together to achieve an image that best explains in a least-square sense the reflection data acquired at receivers. The objective function has the role of comparing observed data with modeled data using the image as reflectivity. In order to achieve the least-squares solution, we employ effiecient gradient methods that decrease the objective function iteratively (Hestenes and Stiefel, 1952; Scales, 1987).

Because of the high computational cost of LSRTM, which is at least an order of magnitude higher than RTM, techniques that expedite LSRTM convergence towards the true reflectivity model lead to reduction in computational cost while also achieving a satisfying solution in fewer iterations. For instance, a common procedure to obtain faster rates of convergence is to use an approximate of the Hessian operator (Aoki and Schuster, 2009; Tang, 2009; Dai et al., 2010; Kazemi and Sacchi, 2015; Huang et al., 2016; Hou and Symes, 2016). Here, we demonstrate that modeling and migration operators based on an imaging condition that delivers more accurate amplitudes and attenuates artifacts, such as the one derived from the energy norm (Douma et al., 2010; Whitmore and Crawley, 2012; Brandsberg-Dahl et al., 2013; Pestana et al., 2013; Rocha et al., 2016) also expedites convergence. This migration operator attenuates low-wavenumber artifacts, delivering a better representation of subsurface reflectivity. The corre-

sponding modeling operator uses spatial and temporal derivatives based on the wave equation itself to generate scattered wavefields from the energy image. We also incorporate preconditioning with an approximation of the Hessian operator in our inversion, which expedites LSRTM convergence even more. This approximation of the Hessian is achieved by a non-stationary multidimensional filter that corrects the blurring effect in the image caused by the wavefield modeling and migration operators (Guitton, 2004; Aoki and Schuster, 2009; Fletcher et al., 2016).

2 THEORY

We can define acoustic wavefield migration as an operator such that

$$\mathbf{m} = \mathbf{L}^{\mathrm{T}}\mathbf{d}_r \ , \tag{1}$$

where $\mathbf{L}^{\mathrm{T}}$ is the migration operator based on some imaging condition, $\mathbf{d}_r$ is single-scattered data recorded at receiver locations, and $\mathbf{m}$ is an image (representing reflectivity). The operator $\mathbf{L}^{\mathrm{T}}$ involves back-propagation of $\mathbf{d}_r$ through an Earth model, thus generating a receiver wavefield $\mathbf{U}_r$, and the application of an imaging condition comparing with a $\mathbf{U}_r$ with the source wavefield $\mathbf{U}_s$. One generally considers the migration operator as the adjoint operator of single-scattering modeling (or commonly known as linearized modeling). Therefore, $\mathbf{L}$ is the linearized modeling operator such that

$$\mathbf{d}_r = \mathbf{L}\mathbf{m} \ , \tag{2}$$

which generates single-scattering data $\mathbf{d}_r$ at receiver locations using an image containing reflectors that act as sources under the action of the source wavefield $\mathbf{U}_s$.

Therefore, we define $\mathbf{m}$ as reflectivity that depends on a certain imaging condition and is not necessarily defined in terms of contrasts in the Earth model. The same principle applies to the linearized modeling operator $\mathbf{L}$, which we define as an adjoint operator to a certain imaging condition, and this operator is not directly related to the physics of single scattering.

2.1 Conventional imaging condition and linearized modeling

The conventional imaging condition is defined as the zero-lag cross-correlation between source and receiver wavefields $\mathbf{U}_s$ and $\mathbf{U}_r$:

$$\mathbf{m} = \left(\mathbf{U}_s\right)^{\mathrm{T}}\mathbf{U}_r \ . \tag{3}$$

Since we know both wavefields are generated by extrapolation using an Earth model and truncated data at receivers, we can rewrite equation 3 as

$$\mathbf{m} = \left(\mathbf{E}_+\mathbf{K}_s\mathbf{d}_s\right)^{\mathrm{T}}\mathbf{E}_-\mathbf{K}_r\mathbf{d}_r \ , \tag{4}$$

where $\mathbf{E}_+$ and $\mathbf{E}_-$ are forward and backward extrapolator operators, and $\mathbf{K_s}$ and $\mathbf{K_r}$ are source and receiver injection operators (see Appendix A), respectively. Note two important relations between the extrapolator operators: $\mathbf{E}_+ = \mathbf{E}_-^{\mathrm{T}}$ and $\mathbf{E}_- = \mathbf{E}_+^{\mathrm{T}}$. Then, one can write equation 4 similarly to equation 1:

$$\mathbf{m} = \mathbf{L}^{\mathrm{T}}\mathbf{d}_r \ , \tag{5}$$

where

$$\mathbf{L}^{\mathrm{T}} = \left(\mathbf{E}_+\mathbf{K}_s\mathbf{d}_s\right)^{\mathrm{T}}\mathbf{E}_-\mathbf{K}_r \ . \tag{6}$$

We can obtain the operator $\mathbf{L}$ (adjoint of $\mathbf{L}^{\mathrm{T}}$) if we apply the adjoint for each individual operator and reverse the order of operators. Therefore, conventional linearized modeling is defined as

$$\mathbf{d}_r = \mathbf{L}\mathbf{m} \ , \tag{7}$$

where

$$\mathbf{L} = \mathbf{K}_r^{\mathrm{T}}\mathbf{E}_+\left(\mathbf{E}_+\mathbf{K}_s\mathbf{d}_s\right) = \mathbf{K}_r^{\mathrm{T}}\mathbf{E}_+\mathbf{U}_s \ . \tag{8}$$

In other words, single-scattered data $\mathbf{d}_r$ are obtained by extraction at the receiver locations ($\mathbf{K}_r^{\mathrm{T}}$), and wavefield extrapolation ($\mathbf{E}_+$) with $\mathbf{U}_s\mathbf{m}$ as the source term.

2.2 Energy imaging condition and linearized modeling

The energy imaging condition for acoustic isotropic wavefields $\mathbf{U}_s$ and $\mathbf{U}_r$ is defined as (Rocha et al., 2016)

$$\mathbf{m} = \left(\Box\mathbf{U}_s\right)^{\mathrm{T}}\Box\mathbf{U}_r \ . \tag{9}$$

Using the operators in equation 4, equation 9 becomes

$$\mathbf{m} = \left(\Box\mathbf{E}_+\mathbf{K}_s\mathbf{d}_s\right)^{\mathrm{T}}\Box\mathbf{E}_-\mathbf{K}_r\mathbf{d}_r \ . \tag{10}$$

Since equation 10 is a function of $\mathbf{d}_r$, we can write the corresponding migration operation as

$$\mathbf{m} = \mathbf{L}^{\mathrm{T}}\mathbf{d}_r \ , \tag{11}$$

where

$$\mathbf{L}^{\mathrm{T}} = \left(\Box\mathbf{E}_+\mathbf{K}_s\mathbf{d}_s\right)^{\mathrm{T}}\Box\mathbf{E}_-\mathbf{K}_r \ . \tag{12}$$

Therefore, the linearized modeling operation based on the energy norm is defined as

$$\mathbf{d}_r = \mathbf{L}\mathbf{m} \ , \tag{13}$$

where

$$\mathbf{L} = \mathbf{K}_r^{\mathrm{T}}\mathbf{E}_+\Box^{\mathrm{T}}\Box\left(\mathbf{E}_+\mathbf{K}_s\mathbf{d}_s\right) = \mathbf{K}_r^{\mathrm{T}}\mathbf{E}_+\Box^{\mathrm{T}}\Box\mathbf{U}_s \ . \tag{14}$$

In other words, single-scattered data $\mathbf{d}_r$ are obtained by extraction at the receiver locations ($\mathbf{K}_r^{\mathrm{T}}$), and wavefield extrapolation ($\mathbf{E}_+$) with $\Box^{\mathrm{T}}\Box\mathbf{U}_s\mathbf{m}$ as the source term, which for a point in space and time can be written explicitly as

$$\begin{aligned}\left[\Box^{\mathrm{T}}\Box\mathbf{U}_s\mathbf{m}\right](\mathbf{x},t) &= \frac{\mathbf{m}(\mathbf{x})}{v^2(\mathbf{x})}\ddot{\mathbf{U}}_s(\mathbf{x},t) - \\ &\nabla\cdot\left[\mathbf{m}(\mathbf{x})\nabla\mathbf{U}_s(\mathbf{x},t)\right] \ ,\end{aligned} \tag{15}$$

The same procedure to find a proper adjoint operator is applicable to other imaging conditions. For instance, applying a Laplacian operator on a conventional image is theoretically equivalent to the application of the energy imaging condition

(Douma et al., 2010). Knowing that the Laplacian operator is self-adjoint, the imaging condition with Laplacian filtering can be written as

$$\mathbf{m} = \nabla^2 \left(\mathbf{U}_s\right)^{\mathrm{T}} \mathbf{U}_r \ . \tag{16}$$

The corresponding linearized modeling is written as

$$\mathbf{d}_r = \mathbf{L}\mathbf{m} \ , \tag{17}$$

where

$$\mathbf{L} = \mathbf{K}_r^{\mathrm{T}} \mathbf{E}_+ \left(\mathbf{E}_+ \mathbf{K}_s \mathbf{d}_s\right) \nabla^2 = \mathbf{K}_r^{\mathrm{T}} \mathbf{E}_+ \mathbf{U}_s \nabla^2 \ . \tag{18}$$

The source term for this case is $\mathbf{U}_s \nabla^2 \mathbf{m}$ and can be written explicitly for each point in space and time as

$$\left[\mathbf{U}_s \nabla^2 \mathbf{m}\right](\mathbf{x}, t) = \mathbf{U}_s(\mathbf{x}, t) \nabla^2 \mathbf{m} \ . \tag{19}$$

2.3 Least-squares migration and preconditioning with an approximation of the Hessian

A pair of linearized modeling and migration operators enables us to compute an image that minimizes the L_2 norm of the difference between observed and modeled data:

$$E(\mathbf{m}) = \frac{1}{2} \|\mathbf{L}\mathbf{m} - \mathbf{d}_r\|^2 \ , \tag{20}$$

and such image is mathematically described by

$$\mathbf{m}^{LS} = \left(\mathbf{L}^{\mathrm{T}} \mathbf{L}\right)^{-1} \mathbf{L}^{\mathrm{T}} \mathbf{d}_r \ . \tag{21}$$

To find $\mathbf{m}^{LS}$, one generally employs iterative procedures that exploit the direction of the gradient of the objective function in equation 20 at a given iteration i:

$$\mathbf{g}_i = \frac{\partial E(\mathbf{m}_i)}{\partial \mathbf{m}_i} = \mathbf{L}^{\mathrm{T}} \left(\mathbf{L}\mathbf{m}_i - \mathbf{d}_r\right) \ , \tag{22}$$

and the model update at each iteration in steepest descent and conjugate gradient methods is a scaled version of the gradient

$$\mathbf{m}_{i+1} = \mathbf{m}_i - \alpha \mathbf{g}_i \ , \tag{23}$$

In equation 21, the term $\mathbf{L}^{\mathrm{T}}\mathbf{L}$ is known as the Hessian operator of $E(\mathbf{m})$. If the inverse of the Hessian is applied to the RTM image $\mathbf{L}^{\mathrm{T}}\mathbf{d}_r$, the least-squares solution is achieved. However, in practice, the Hessian operator cannot be explicitly computed for least-squares migration problems. As suggested by Guitton (2004), we can obtain an approximation of the Hessian operator if we compute an image

$$\mathbf{m}_1 = \mathbf{L}^{\mathrm{T}} \mathbf{L} \mathbf{m}_0 \ , \tag{24}$$

where $\mathbf{m}_0 = \mathbf{L}^{\mathrm{T}} \mathbf{d}_r$ is the standard RTM image. The operator $\mathbf{B}$ that minimizes

$$\|\mathbf{m}_0 - \mathbf{B}\mathbf{m}_1\|^2 \ , \tag{25}$$

is a good approximation of the inverse of the Hessian $\left(\mathbf{L}^{\mathrm{T}}\mathbf{L}\right)^{-1}$ according to equation 24. We can define the operator $\mathbf{B}$ as a multidimensional convolutional operator in along all spatial axes.

Once we obtain the approximation of the inverse of the Hessian, we can expedite convergence in least-squares inversion by preconditioning the gradient with the operator $\mathbf{B}$ before updating the model at each iteration. Incorporating the preconditioning, equation 23 becomes

$$\mathbf{m}_{i+1} = \mathbf{m}_i - \alpha \mathbf{B} \mathbf{g}_i \ , \tag{26}$$

3 EXAMPLES

In order to show how LSRTM with proper imaging operators can get faster convergence rates relative to conventional methods, we perform a LSRTM experiment using a 2D Gulf of Mexico (GOM) dataset, used by many authors in the past as a benchmark dataset (Dragoset, 1999; Guitton and Cambois, 1999; Hadidi et al., 1999; Lamont et al., 1999; Lokshtanov, 1999; Verschuur and Prein, 1999), and described by Guitton et al. (2012). Standard pre-processing is applied to the dataset prior to LSRTM, such as surface-related multiple suppression. We use 71 of the original 1001 shot records, with the first source location at $x = 4000$m and the last at $x = 22670$m, resulting in a source spacing of approximately 267m. The shot decimation decreases the computational cost of the entire experiment but also introduces truncation artifacts, which are useful to test the effectiveness of the proposed LSRTM in attenuating acquisition artifacts. A standard RTM migration (Figure 1(a)) exhibits low-wavenumber artifacts and poor illumination in the subsalt area. We test two alternative LSRTM's, one using modeling and migration with the Laplacian operator (equations 16 and 18), and the other based on the energy norm (equations 12 and 14). For this experiment, the final images from the Laplacian and energy LSRTM's are similar in quality and resolution, and we show the final energy LSRTM image in Figure 1(b). Also, the objective functions (Figure 1(c)) of both alternative LSRTM's decrease faster than the one from conventional LSRTM, with the one based on the energy norm decreasing slightly faster when compared to its Laplacian counterpart. Although the two alternative LSRTM's are theoretically equivalent, the discretization in wavefield extrapolation imposes more loss of accuracy of the numerical derivatives in image domain compared to wavefield domain. As suggested, the energy migration and modeling operators applied either on wavefield domain (equation 15) or on image domain in the form of a Laplacian operator provide faster convergence rates towards the final reflectivity model.

We apply our method to a 3D ocean-bottom node (OBN) dataset from the Gulf of Mexico. We process the dataset to obtain only the down-going pressure component and perform mirror imaging (Godfrey et al., 1998; Ronen et al., 2005) of shallow geological structures. We use 37 node gathers with sources densely distributed at the water surface (Figure 2(a)), and the velocity model used in shown in Figure 2(b). Based on the fact that conventional LSRTM has a worse performance in the preceding example, we perform three LSRTM experiments: Laplacian based LSRTM, energy-norm based LSRTM with and without preconditioning. The energy LSRTM has a slightly smaller objective function value over iterations compared to its Laplacian counterpart, similarly to the preceding example. We compute the matching filter for the precon-

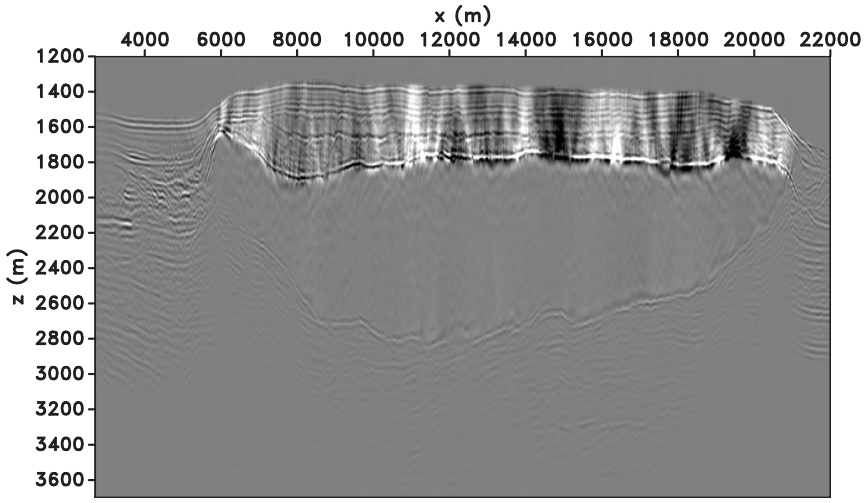

(a)

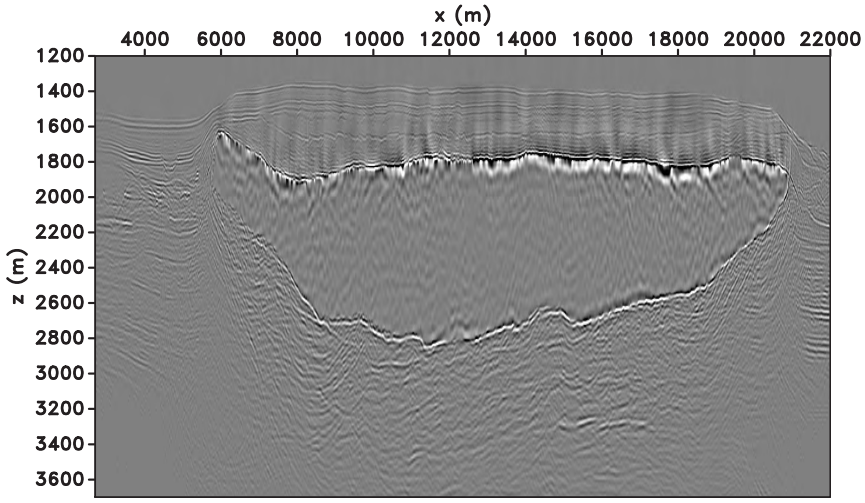

(b)

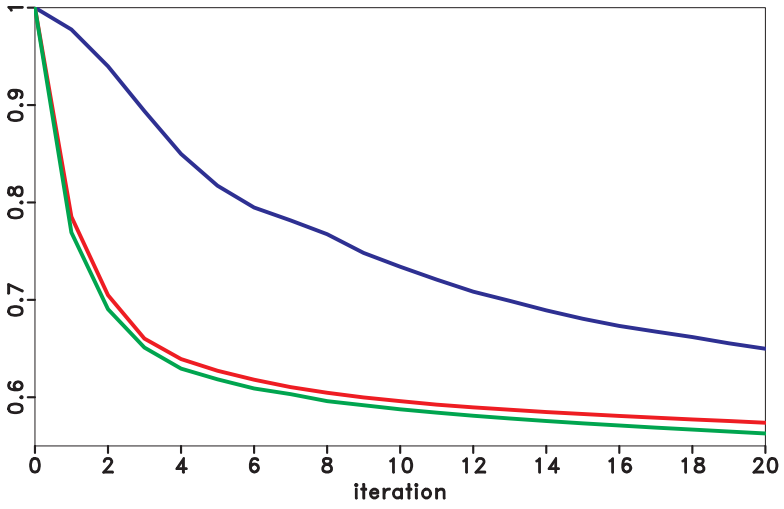

(c)

Figure 1. (a) Conventional RTM image and (b) LSRTM image with the energy modeling and migration operators. (c) Normalized objective functions for conventional LSRTM (blue), LSRTM with Laplacian (red) and based on the energy norm (green). Note the convergence speed-up obtained by the alternative LSRTM's.

ditioning using the energy RTM image $\mathbf{m}_0 = \mathbf{L}^T\mathbf{d}_r$ and $\mathbf{m}_1 = \mathbf{L}^T\mathbf{L}\mathbf{m}_0$, where the modeling ($\mathbf{L}$) and migration ($\mathbf{L}^T$) operators are based on the energy norm. We use the preconditioning at the two first iterations and switch it off at the second iteration, since the matching filter is based on the image at the first iteration (energy RTM image), and is not effective for images at later iterations. However, we obtain a significant speed-up in the convergence rate over all iterations just by applying the preconditioning at the first iterations. The image in Figure 3 compares the RTM and LSRTM images side-by-side, and shows the increase in illumination and frequency content (especially towards low frequencies) in the LSRTM image. Figure 4 compares observed and predicted data at the last iteration, and the difference (residual) between the two for a gather of traces sorted by increasing offset at a particular node location ($x = 214.5$km, $y = 44.9$km). Note that the main reflections at near- and mid-offsets are correctly predicted, but the far-offset amplitudes are not matched mainly because of anisotropy, which is not being accounted for by our acoustic imaging operators. With a number of iterations corresponding to two orders of magnitude of the standard RTM computational cost, we obtain LSRTM images that exhibit more focused diffractions and delineated structures, as shown by the depth slices in Figure 5.

4 CONCLUSIONS

We demonstrate that using proper linearized modeling and migration operators expedites LSRTM, which otherwise suffers from high computational cost. We test modeling and migration operators based on the energy norm, and we obtain faster convergence rates for LSRTM inversion, since the energy operators attenuate artifacts that do not properly characterize subsurface reflectivity. In addition, a preconditioning operator that utilizes a multidimensional non-stationary matching filter decreases the objective function substantially at the first iterations, allowing a significant speed-up for the following iterations. Our field data examples show significant image quality improvement within less than 10 inversion iterations by using an accelerated LSRTM compared to regular RTM.

5 ACKNOWLEDGMENTS

We thank the sponsors of the Center for Wave Phenomena, whose support made this research possible. We are grateful to Shell Exploration and Production Company for permission to publish the results using the 3D Gulf of Mexico dataset. We would like to thank John Kimbro at Shell for helping us with the 3D dataset. The reproducible numeric examples in this paper use the Madagascar open-source software package (Fomel et al., 2013) available at http://www.ahay.org.

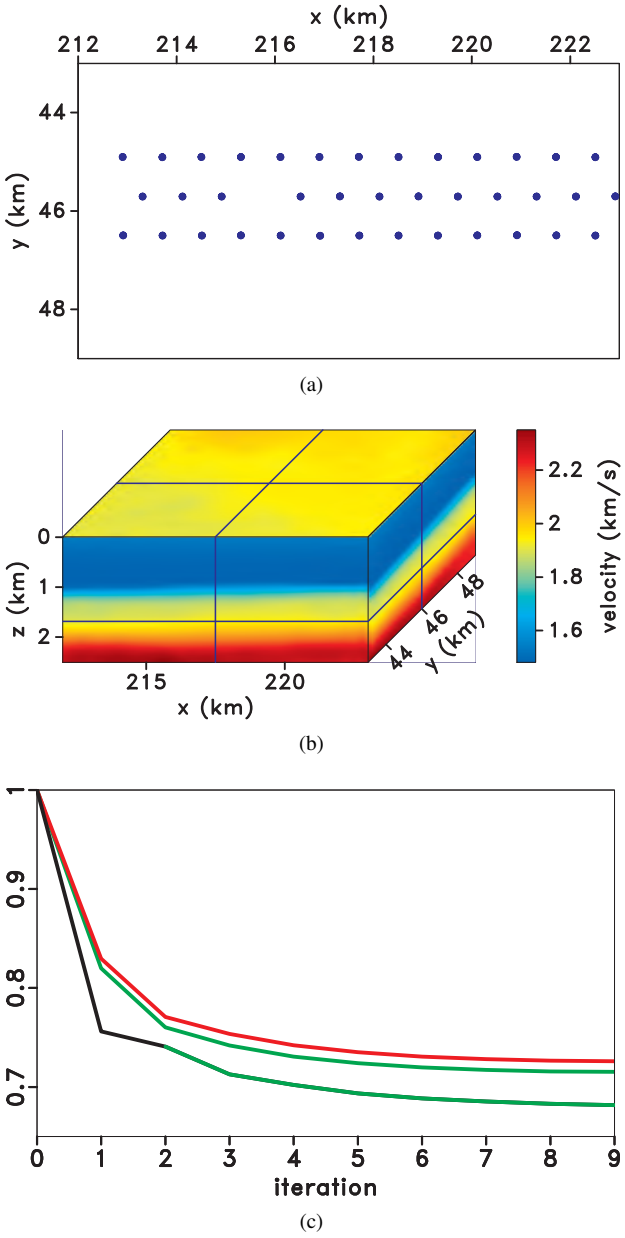

Figure 2. GOM 3D dataset: (a) 37 nodes spaced by approximately 800m, and sources densely distributed at the surface of the model. (b) Velocity model. (c) Normalized objective functions for Laplacian-based (red), energy-based (green), and preconditioned energy-based (black and then green at iteration 2) LSRTM's. The energy LSRTM has best performance if we apply preconditioning at the first two iterations, and then not apply it at the subsequent iterations.

REFERENCES

Aoki, N., and G. T. Schuster, 2009, Fast least-squares migration with a deblurring filter: Geophysics, **74**, no. 6, WCA83–WCA93.

Baysal, E., D. D. Kosloff, and J. W. C. Sherwood, 1983, Reverse time migration: Geophysics, **48**, 1514–1524.

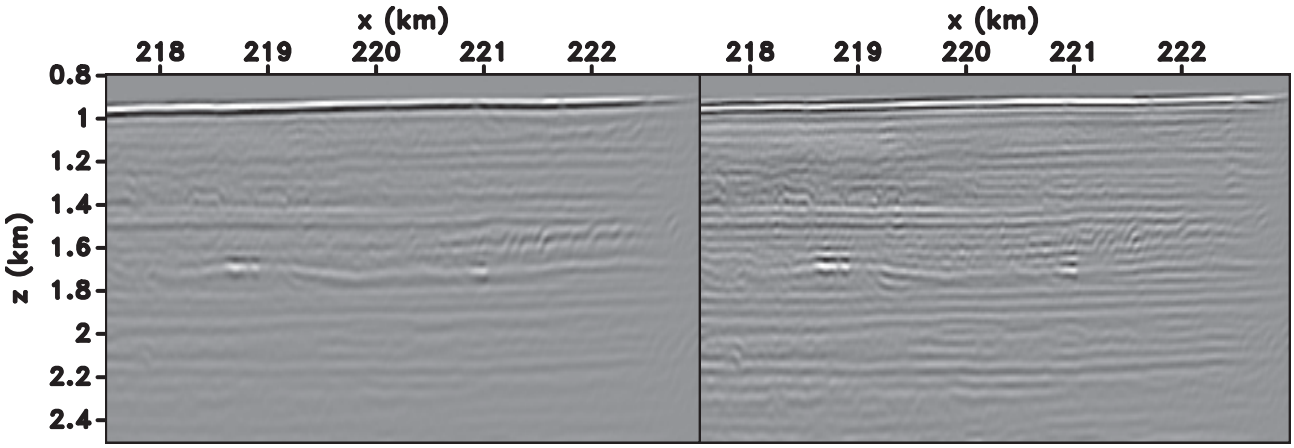

Figure 3. GOM 3D dataset: energy RTM (left) and LSRTM (right) images for the inline section at $y = 44.9$km. Note the increase in frequency content and illumination for the LSRTM image compared to RTM.

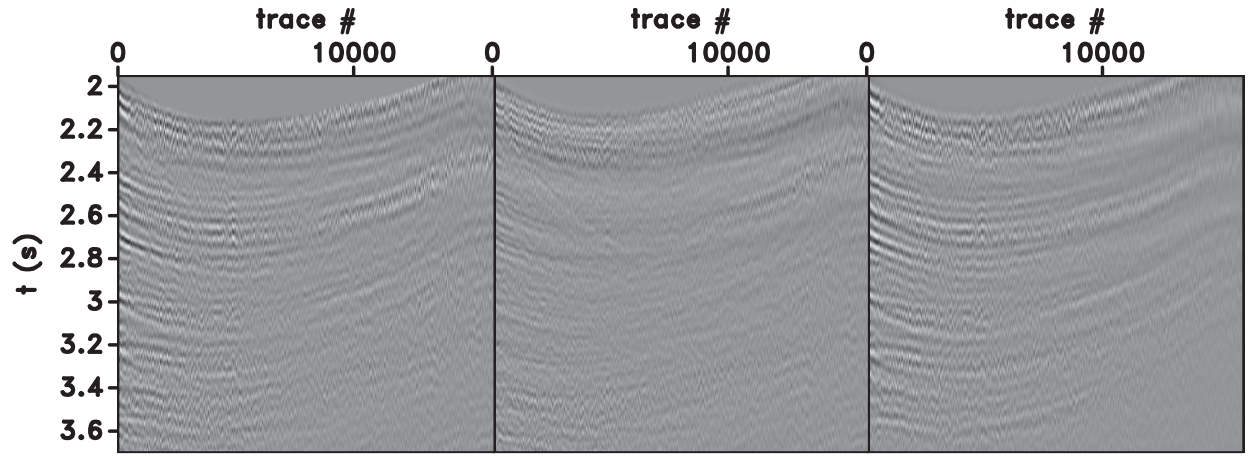

Figure 4. GOM 3D dataset. Node gather at $x = 214.5$km and $y = 44.9$km sorted by increasing offset: (left) observed, (middle) final residual and (right) final modeled data. Note that the main reflection events are predicted and eliminated in the data residual, especially for events at near- and mid-offsets. Linear moveout is applied on these plots for display purposes.

Biondi, B., 2012, 3D Seismic Imaging: Society of Exploration Geophysicists.

Brandsberg-Dahl, S., N. Chemingui, D. Whitmore, S. Crawley, E. Klochikhina, and A. Valenciano, 2013, 3D RTM angle gathers using an inverse scattering imaging condition: 83rd Annual International Meeting, SEG, Expanded Abstracts, 3958–3962.

Chavent, G., and R.-E. Plessix, 1999, An optimal true–amplitude least–squares prestack depth–migration operator: Geophysics, **64**, 508–515.

Claerbout, J. F., 1992, Earth soundings analysis: Processing versus inversion: Blackwell Scientific Publications.

Dai, W., C. Boonyasiriwat, and G. Schuster, 2010, 3D multisource least-squares reverse-time migration: 80th Annual International Meeting, SEG, Expanded Abstracts, 3120–3124.

Dai, W., and G. T. Schuster, 2012, Plane-wave Least-squares Reverse Time Migration: 82rd Annual International Meeting, SEG, Expanded Abstracts.

Dong, S., J. Cai, M. Guo, S. Suh, Z. Zhang, B. Wang, and Z. Li, 2012, Least-squares reverse time migration: towards true amplitude imaging and improving the resolution: 82rd Annual International Meeting, SEG, Expanded Abstracts.

Douma, H., D. Yingst, I. Vasconcelos, and J. Tromp, 2010, On the connection between artifact filtering in reverse-time migration and adjoint tomography: Geophysics, **75**, S219–S223.

Dragoset, B., 1999, A practical approach to surface multiple attenuation: The Leading Edge, **18**, 104–108.

Fletcher, R. P., D. Nichols, R. Bloor, and R. T. Coates, 2016,

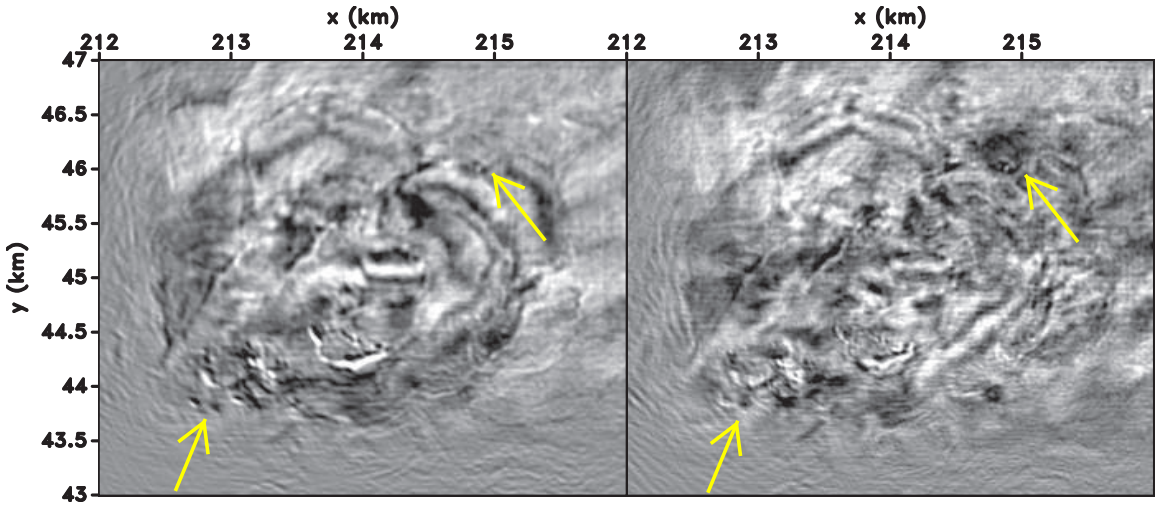

(a)

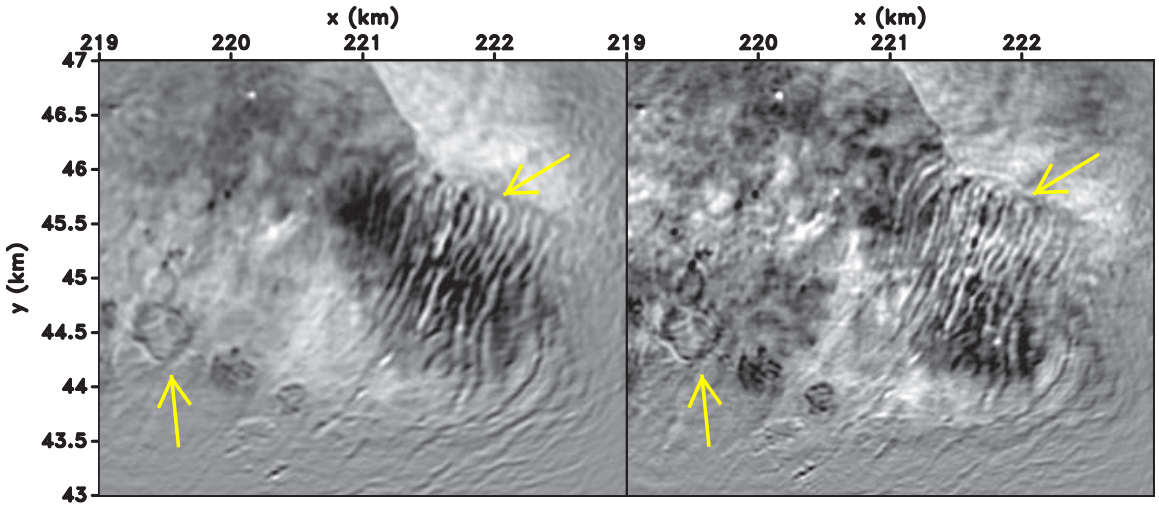

(b)

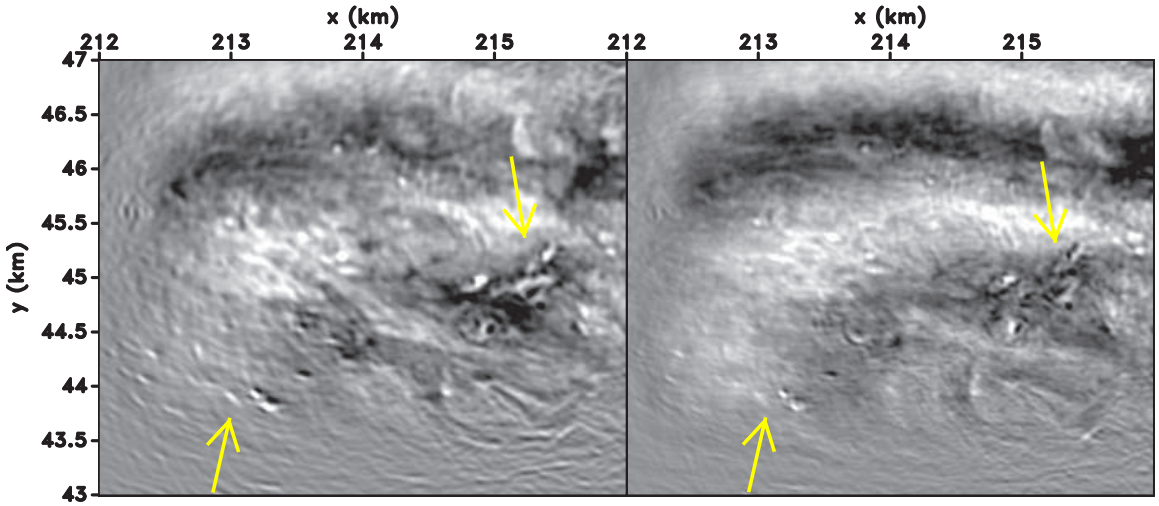

(c)

Figure 5. GOM 3D dataset: RTM (left) and LSRTM (right) images at (a) $z = 1.20$km, (b) 1.55km, (c) and 1.77km. The arrows indicate the greatest improvement in focusing of the diffractors and in delineation of the reflectors.

Least-squares migration : Data domain versus image domain using point spread functions: The Leading Edge, **35**, no. 2, 157–162.

Fomel, S., P. Sava, I. Vlad, Y. Liu, and V. Bashkardin, 2013, Madagascar: open-source software project for multidimensional data analysis and reproducible computational experiments: Journal of Open Research Software, 1:e8, DOI: http://dx.doi.org/10.5334/jors.ag.

Godfrey, R., P. Kristiansen, B. Armstrong, M. Copper, and E. Thorogood, 1998, Imaging the Foinaven ghost: 68th Annual International Meeting, SEG, Expanded Abstracts, 1333–1335.

Guitton, A., 2004, Amplitude and kinematic corrections of migrated images for nonunitary imaging operators: Geophysics, **69**, no. 4, 1017–1024.

Guitton, A., G. Ayeni, and E. Daz, 2012, Constrained full–waveform inversion by model reparameterization: Geophysics, **77**, R117–R127.

Guitton, A., and G. Cambois, 1999, Multiple elimination using a pattern–recognition technique: The Leading Edge, **18**, 92–98.

Hadidi, M. T., M. Sabih, D. E. Johnston, and C. Calderon-Macias, 1999, Mobil's results for the 1997 workshop on multiple attenuation: The Leading Edge, **18**, 100–103.

Hestenes, M. R., and E. Stiefel, 1952, Methods of Conjugate Gradients for Solving Linear Systems: Journal of Research of the National Bureau of Standards, **49**, no. 6, 409–436.

Hou, J., and W. W. Symes, 2016, Accelerating extended least-squares migration with weighted conjugate gradient iteration: Geophysics, **81**, no. 4, S165–S179.

Huang, W., P. Deng, and H.-W. Zhou, 2016, Least-squares reverse-time migration with hessian preconditioning: 86th Annual International Meeting, SEG, Expanded Abstracts, 1043-1046.

Kazemi, N., and M. D. Sacchi, 2015, Block row recursive least-squares migration: Geophysics, **80**, no. 5, A95–A101.

Kuhl, H., and M. D. Sacchi, 2003, Least-squares wave-equation migration for AVO/AVA inversion: Geophysics, **68**, 262–273.

Lailly, P., 1983, The seismic inverse problem as a sequence of before stack migrations: Conference on Inverse Scattering, Theory and Application: Society of Industrial and Applied Mathematics, Expanded Abstracts, 206–220.

Lamont, M. G., B. M. Hartley, and N. F. Uren, 1999, Multiple attenuation using the MMO and ISR preconditioning transforms: The Leading Edge, **18**, 110–114.

Levin, S. A., 1984, Principle of reverse-time migration: Geophysics, **49**, 581–583.

Lokshtanov, D., 1999, Multiple suppression by data–consistent deconvolution: The Leading Edge, **18**, 115–119.

McMechan, G. A., 1983, Migration by extrapolation of time dependent boundary values: Geophysical Prospecting, **31**, 413–420.

Nemeth, T., C. Wu, and G. T. Schuster, 1999, Least–squares migration of incomplete reflection data: Geophysics, **64**, 208–221.

Pestana, R., A. W. G. dos Santos, and E. S. Araujo, 2013, RTM imaging condition using impedance sensitivity kernel combined with Poynting vector: 13th International Congress of The Brazilian Geophysical Society.

Rocha, D., N. Tanushev, and P. Sava, 2016, Acoustic wavefield imaging using the energy norm: Geophysics, **81**, no. 4, S151–S163.

Ronen, S., L. Comeaux, and X.-G. Miao, 2005, Imaging downgoing waves from ocean bottom stations: 75th Annual International Meeting, SEG, Expanded Abstracts, 963–967.

Scales, J., 1987, Tomographic inversion via the conjugate gradient method: Geophysics, **52**, 179–185.

Sun, J., Y. Zhang, S. Gray, C. Notfors, and J. Young, 2003, 3-D prestack depth migration by wavefield extrapolation methods: ASEG Extended Abstracts 2003, pp 1-4.

Tang, Y., 2009, Target-oriented wave-equation least-squares migration/inversion with phase–encoded hessian: Geophysics, **74**, no. 6, WCA95–WCA107.

Verschuur, D. J., and R. J. Prein, 1999, Multiple removal results from Delft University: The Leading Edge, **18**, 86–91.

Whitmore, N. D., and S. Crawley, 2012, Application of RTM inverse scattering imaging conditions: 82nd Annual International Meeting, SEG, Expanded Abstracts, 1–6.

Yao, G., and H. Jakubowicz, 2012, Least-Squares Reverse-Time Migration: 82rd Annual International Meeting, SEG, Expanded Abstracts.

Zhang, Y., L. Duan, and Y. Xie, 2015, A stable and practical implementation of least-squares reverse time migration: Geophysics, **80**, no. 1, V23–V31.

Zhang, Y., and J. Sun, 2009, Practical issues in reverse time migration: true amplitude gathers, noise removal and harmonic source enconding: First Break, **27**, 53–59.

Appendix A

Conventional migration and modeling operators

For source and receiver wavefields $\mathbf{U}_s\left(\mathbf{x},t\right)$ and $\mathbf{U}_r\left(\mathbf{x},t\right)$, an image $\mathbf{m}\left(\mathbf{x}\right)$ is conventionally obtained by

$$\mathbf{m}=\left(\mathbf{U}_s\right)^{\mathrm{T}}\mathbf{U}_r\ . \tag{A.1}$$

We can represent equation A.1 and the following equations pictorially using matrices, which indicate the relative dimensions of operators and variables:

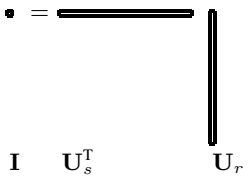

By using forward and backward extrapolator operators $\mathbf{E}_+\left(\mathbf{x},t\right)$ and $\mathbf{E}_-\left(\mathbf{x},t\right)$, and source and receiver injection operators $\mathbf{K_s}\left(\mathbf{x},\mathbf{x}_s,t\right)$ and $\mathbf{K_r}\left(\mathbf{x},\mathbf{x}_r,t\right)$, we have

$$\mathbf{m}=\left(\mathbf{E}_+\mathbf{K}_s\mathbf{d}_s\right)^{\mathrm{T}}\mathbf{E}_-\mathbf{K}_r\mathbf{d}_r\ , \tag{A.2}$$

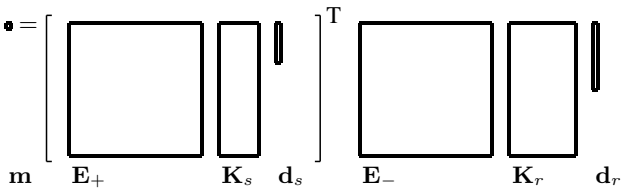

where $\mathbf{d}_s(\mathbf{x}_s, t)$ and $\mathbf{d}_r(\mathbf{x}_r, t)$ are the source and receiver data, respectively. In compact form, we can rewrite equation A.2 as

$$\mathbf{m} = \mathbf{L}^{\mathrm{T}}\mathbf{d}_r \ . \tag{A.3}$$

Linearized modeling is defined as

$$\mathbf{d}_r = \mathbf{L}\mathbf{m} \tag{A.4}$$

Based on equations A.2 and A.3, we can rewrite equation A.4 as

$$\mathbf{d}_r = \mathbf{K}_r^{\mathrm{T}}\mathbf{E}_-^{\mathrm{T}}\mathbf{U}_s\mathbf{m} \ , \tag{A.5}$$

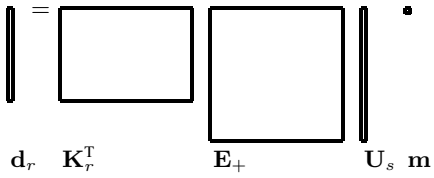

or

$$\mathbf{d}_r = \mathbf{K}_r^{\mathrm{T}}\mathbf{E}_+\left(\mathbf{E}_+\mathbf{K}_s\mathbf{d}_s\right)\mathbf{m} \ , \tag{A.6}$$

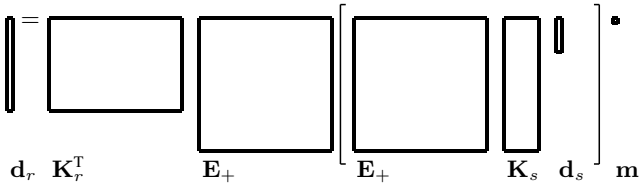

where $\mathbf{E}_-^{\mathrm{T}} = \mathbf{E}_+$, and $\mathbf{K}_r^{\mathrm{T}}$ represents the extraction at the receiver locations (adjoint operator of the injection operator).

Appendix B

Energy migration and modeling operators

The energy image $\mathbf{m}(\mathbf{x})$ is obtained by

$$\mathbf{m} = \left(\square\mathbf{U}_s\right)^{\mathrm{T}}\square\mathbf{U}_r \ . \tag{B.1}$$

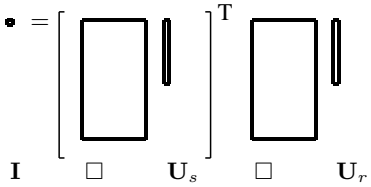

The operator $\square$ turns an acoustic wavefield into a vector field whose components are spatial and temporal. We represent this increase in dimensions pictorially by making the matrix of $\square$ considerably larger than the wavefields matrices. Using extrapolator and injection operators, we have

$$\mathbf{m} = \left(\square\mathbf{E}_+\mathbf{K}_s\mathbf{d}_s\right)^{\mathrm{T}}\square\mathbf{E}_-\mathbf{K}_r\mathbf{d}_r \ , \tag{B.2}$$

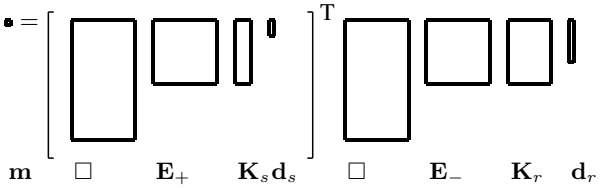

In compact form, we can rewrite equation B.2 as

$$\mathbf{m} = \mathbf{L}^{\mathrm{T}}\mathbf{d}_r \ , \tag{B.3}$$

Linearized modeling is defined as

$$\mathbf{d}_r = \mathbf{L}\mathbf{m} \tag{B.4}$$

Based on equations B.2 and B.3, we can rewrite equation B.4 as

$$\mathbf{d}_r = \mathbf{K}_r^{\mathrm{T}}\mathbf{E}_-^{\mathrm{T}}\square^{\mathrm{T}}\square\mathbf{U}_s\mathbf{m} \ , \tag{B.5}$$

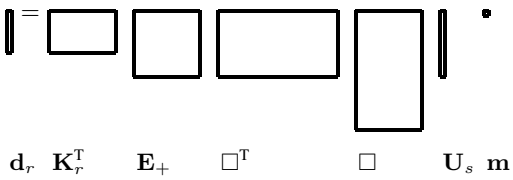

or

$$\mathbf{d}_r = \mathbf{K}_r^{\mathrm{T}}\mathbf{E}_+\square^{\mathrm{T}}\square\left(\mathbf{E}_+\mathbf{K}_s\mathbf{d}_s\right)\mathbf{m} \ . \tag{B.6}$$